The Astrophysical Journal, 919:28 (5pp), 2021 September 20 https://doi.org/10.3847/1538-4357/ac18c0


# Two-dimensional Particle-in-cell Simulation of Magnetic Reconnection in the Downstream of a Quasi-perpendicular Shock

Quanming Lu[1,2], Zhongwei Yang[3], Huanyu Wang[1,2], Rongsheng Wang[1,2], Kai Huang[1,2], San Lu[1,2], and Shui Wang[1,2]
[1] CAS Key Lab of Geospace Environment, School of Earth and Space Sciences, University of Science and Technology of China, Hefei 230026, People's Republic of China; qmlu@ustc.edu.cn
[2] CAS Center for Excellence in Comparative Planetology, People's Republic of China
[3] State Key Laboratory of Space Weather, National Space Science Center, Chinese Academy of Sciences, Beijing, 100190, People's Republic of China zwyang@swl.ac.cn
*Received 2021 May 3; revised 2021 July 26; accepted 2021 July 27; published 2021 September 21*

## Abstract

In this paper, by performing a two-dimensional particle-in-cell simulation, we investigate magnetic reconnection in the downstream of a quasi-perpendicular shock. The shock is nonstationary, and experiences cyclic reformation. At the beginning of the reformation process, the shock front is relatively flat, and part of the upstream ions are reflected by the shock front. The reflected ions move upward in the action of the Lorentz force, which leads to the upward bending of the magnetic field lines at the foot of the shock front, and then a current sheet is formed due to the squeezing of the bending magnetic field lines. The formed current sheet is brought toward the shock front by the solar wind, and the shock front becomes irregular after interacting with the current sheet. Both the current sheet carried by the solar wind and the current sheet associated with the shock front are then fragmented into many small filamentary current sheets. Electron-scale magnetic reconnection may occur in several of these filamentary current sheets when they are convected into the downstream, and magnetic islands are generated. A strong reconnection electric field and energy dissipation are also generated around the X line, and a high-speed electron outflow is also formed.

*Unified Astronomy Thesaurus concepts:* Space plasmas (1544); Plasma physics (2089); Solar magnetic reconnection (1504); Planetary bow shocks (1246)

*Supporting material:* animation

## 1. Introduction

Collisionless magnetic reconnection plays an important role in the Earth's magnetosphere, and two sites where magnetic reconnection can often be observed are the dayside magnetopause and magnetotail. In the dayside magnetopause, magnetic reconnection occurs when the interplanetary magnetic field has a southern component, and plasma energy in the solar wind enters the magnetosphere through magnetic reconnection (e.g., Dungey 1961; Paschmann et al. 1979; Pu et al. 2007). Magnetic reconnection in the magnetotail explosively releases the stored magnetic energy in the lobe, and causes substorms (e.g., Baker et al. 2002; Angelopoulos et al. 2008; Lu et al. 2020b). Recently, with the availability of high-resolution satellite observations, the transition region or magnetosheath downstream of the bow shock is evidenced to be another site, where reconnection can be often observed in the magnetosphere (Retinò et al. 2007; Vörös et al. 2017; Yordanova et al. 2016; Phan et al. 2018; Wang et al. 2018).

The bow shock is formed after the high-speed solar wind interacts with the Earth's magnetosphere, and the magnetosheath behind the shock is usually in a turbulent state. According to the shock normal angle ($\theta_{Bn}$) between the shock normal and the upstream magnetic field, the bow shock can be separated into a quasi-parallel shock ($\theta_{Bn} < 45°$) and quasi-perpendicular shock ($\theta_{Bn} > 45°$), and their characteristics are quite different. In the quasi-parallel shock, the ions that are reflected by the shock can move into the far upstream and excite low-frequency large-amplitude electromagnetic waves due to plasma beam instabilities (e.g., Su et al. 2012; Scholer 1990; Hao et al. 2016). With a global three-dimensional (3D) hybrid simulation model, Lu et al. (2020a) found that, when these waves are convected toward the shock by the solar wind, they evolve into current sheets after penetrating the shock. Magnetic reconnection can occur in these current sheets, and magnetic islands may be generated. By performing a local two-dimensional (2D) particle-in-cell (PIC) simulation, Bessho et al. (2019) found that magnetic reconnection can also occur in the transition region of a quasi-parallel shock. In situ evidence of magnetic reconnection in the magnetosheath downstream of a quasi-parallel shock has also been provided by Cluster and Magnetospheric Multiscale (MMS) satellite observations (Retinò et al. 2007; Phan et al. 2018; Yordanova et al. 2016; Vörös et al. 2017).

In a perpendicular shock, the ions that are reflected by the shock quickly transmit to the downstream (Hada et al. 2003; Johlander et al. 2016; Yang et al. 2020a; Turner et al. 2021), with an anisotropic distribution in which the perpendicular temperature is larger than the parallel temperature, and then excite ion cyclotron waves and mirror waves (e.g., McKean et al. 1992; Lu & Wang 2006; Winske & Quest 1988; Hao et al. 2014). However, there is some evidence indicating the existence of magnetic reconnection in the transition region of a quasi-perpendicular shock (Wang et al. 2019). In this paper, with the help of a 2D PIC simulation model, we try to figure out the mechanism for the formation of current sheets and consequential magnetic reconnection in a quasi-perpendicular shock.

## 2. Simulation Model

An open-source electromagnetic 2D PIC simulation code named EPOCH (Arber et al. 2015) is used in this article to study magnetic reconnection in a perpendicular shock. The

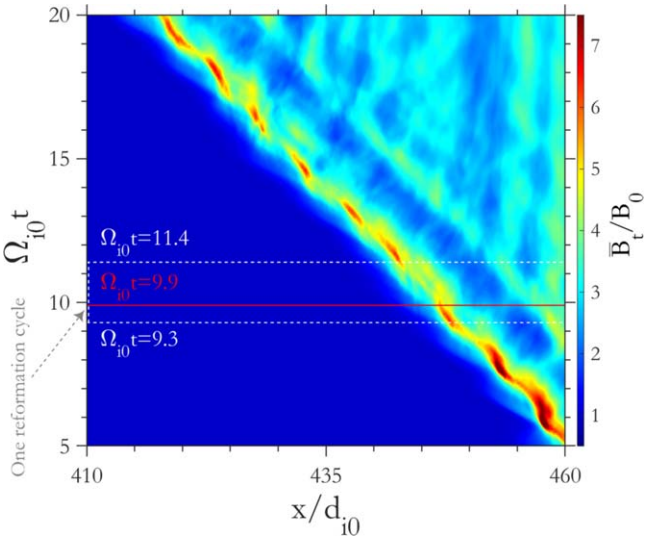


**Figure 1.** Evolution of the perpendicular shock by plotting the stacked profiles of the magnetic field $\bar{B}_t$ from $\Omega_{i0}t = 5$ to 20. Here, $\bar{B}_t$ is the average value of the magnetic field $B_t = \sqrt{B_x^2 + B_y^2 + B_z^2}$ over the $z$ direction.

shock is formed by the injection method (Matsukiyo & Scholer 2012), where particles are injected from the left side of the simulation boundary (at $x = 0$) at a speed $V_{\rm in} = 7V_{\rm A0}$ (where $V_{\rm A0}$ is the Alfvén speed based on the upstream plasma density $n_0$ and magnetic field $B_0$), and a specular reflection for particles is used in the right boundary ($x = L_x$, where $L_x$ is the size of the simulation domain in the $x$ direction). The formed shock propagates toward the left (the $-x$ direction). The 2D simulation is performed in the $x-z$ plane, and the ambient magnetic field is $\boldsymbol{B}_0 = B_0(\cos\theta_{Bn}\boldsymbol{i_x} - \sin\theta_{Bn}\boldsymbol{i}_y)$, where $\theta_{Bn}$ is the shock normal angle. In our simulation, we choose $\theta_{Bn} = 60^0$; therefore, the shock is quasi-perpendicular. Here, the ambient magnetic field has a strong component perpendicular to the simulation plane, as in (Lembege & Savoini 1992; Yang et al. 2012; Yang et al. 2020b). Periodic boundary conditions for both electromagnetic fields and particles are applied in the $z$ direction.

The domain size of the simulation is $L_x \times L_z = 470.4d_{i0} \times 12d_{i0}$, where $d_{i0} = c/\omega_{pi0}$ is the ion inertial length, and $\omega_{pi0} = \sqrt{n_0 e^2/m_i\varepsilon_0}$ is the ion plasma frequency based on the upstream plasma density $n_0$. The grid number is $n_x \times n_z = 47,040 \times 1200$, and the grid size is $\Delta x = \Delta z = 0.01d_{i0}$. Initially, there are 50 ions and electrons in every cell, and the ion-to-electron mass ratio is $m_i/m_e = 64$. The light speed is $c/V_{\rm A0} = 28$. The plasma beta values in the upstream are $\beta_{i0} = 0.1$ and $\beta_{e0} = 0.2$.

## 3. Simulation Results

The shock is formed due to the interaction of the injected plasma from the left boundary and the plasma reflected from the right boundary, and its front propagates from right to left. Figure 1 describes the evolution of the perpendicular shock by plotting the stacked profiles of the magnetic field $\bar{B}_t$ from $\Omega_{i0}t = 5$ to 20. During this time period, the shock front is already sufficiently away from the right boundary, and influence from the right boundary can be negligible. Here, $\bar{B}_t$ is the average value of the magnetic field $B_t = \sqrt{B_x^2 + B_y^2 + B_z^2}$ over the $z$ direction. The propagation speed of the shock front is about $2.5V_{\rm A0}$, and then the Alfvén Mach number is about 9.5 in the shock frame. The reformation of the shock front can be clearly identified in the figure, as demonstrated by the cyclic variations in the magnetic field $\bar{B}_t$ in the shock front. The reformation period is estimated to be about $2.1\Omega_i^{-1}$. It is generally considered that the reformation of the shock front is related to the ions that are reflected by the shock (e.g., Lembege & Savoini 2002; Yang et al. 2009). The reflected ions are accumulated in the foot, and then the foot amplitude increases until it exceeds that of the shock front. Finally, a new shock front is formed, and the old shock front becomes gradually weaker.

The reformation process of the shock front is exhibited more clearly in Figure 2, which shows the magnetic field lines and electron current in the $y$ direction ($j_{ey}$) at $\Omega_{i0}t = 9.3$, 9.7, 9.9, 10.7, 11.1, and 11.4. The profiles of the average value of the magnetic field $\bar{B}_t$ at these times are also plotted in the figure for reference. These time slots are selected from one reformation period (from about $\Omega_{i0}t = 9.3$ to 11.4). At $\Omega_{i0}t = 9.3$, the shock front is relatively flat, and it is located at $x \approx 446d_{i0}$. There exists strong electron currents associated with the shock front. Part of the upstream ions are reflected by the shock front, and they will move upward in the action of the Lorentz force, which drags the magnetic field lines at the foot region and bends them upward. Then, the bending magnetic field lines are squeezed. Finally, a current sheet is formed, where the current is carried mainly by the electrons and points to the $+y$ direction when the current sheet is convected toward the shock front by the solar wind. The interaction of these structures with the shock front causes local curvature variations in the shock front, and a rippled shock front is formed. From the profile of the average value of the magnetic field $\bar{B}_t$, we can identify the enhancement of the magnetic field in the foot region of the shock. Simultaneously, both the current sheet carried by the solar wind and the current sheet associated with the shock front are distorted, and several magnetic islands are generated in the foot region and downstream. When these structures are fully merged with the shock front, the enhancement of the magnetic field surpasses that of the shock front, and a new shock front is eventually formed. A new cycle of shock reformation begins again.

The generation of magnetic islands in the distorted currents sheets in the foot region and downstream of the shock indicates the occurrence of magnetic reconnection. This can be demonstrated more clearly in Figure 3. In Figure 3, we plot the enlarged view of the region denoted by the red lines in Figure 2(c). Figures 3(a)–(d) present the electron current in the $y$ direction $j_{ey}$, the fluctuating magnetic field in the $y$ direction $\delta B_y$ (where $\delta B_y = B_y - \tilde{B}_y$, and $\tilde{B}_y$ is the average value of $B_y$ in the denoted region), the electric field in the $y$ direction $E_y'$ (where $\boldsymbol{E}' = \boldsymbol{E} + \boldsymbol{V_e} \times \boldsymbol{B}$), and $j_{ey}E_y'$ at $\Omega_{i0}t = 9.9$, respectively. The magnetic field lines are also plotted in these figures for reference. There are several strong electron current sheets in the region, and we focus on the two strong electron current sheets denoted by CS1 and CS2. We have also transformed the two current sheets into the local current sheet coordinate system, i.e., ($L_1$, $M_1$, $N_1$) and ($L_2$, $M_2$, $N_2$), through minimum variance analysis (Sonnerup & Scheible 1998), and $\boldsymbol{L_1} = (0.585, 0, 0.81)$ and $\boldsymbol{L_2} = (0.842, 0, 0.538)$. The currents are directed toward the $+y$ and $-y$ directions in current sheets CS1 and CS2, respectively, and an X-type configuration of the magnetic field lines is formed in every current sheet. The half-widths of the current sheets are estimated to be about $0.19d_{i0}$ and $0.11d_{i0}$ around the X lines, while their lengths are about $0.28d_{i0}$ and $0.36d_{i0}$. The fluctuating magnetic field $\delta B_y$ is produced around the two X lines. Here, the fluctuating magnetic field $\delta B_y$ does not exhibit the

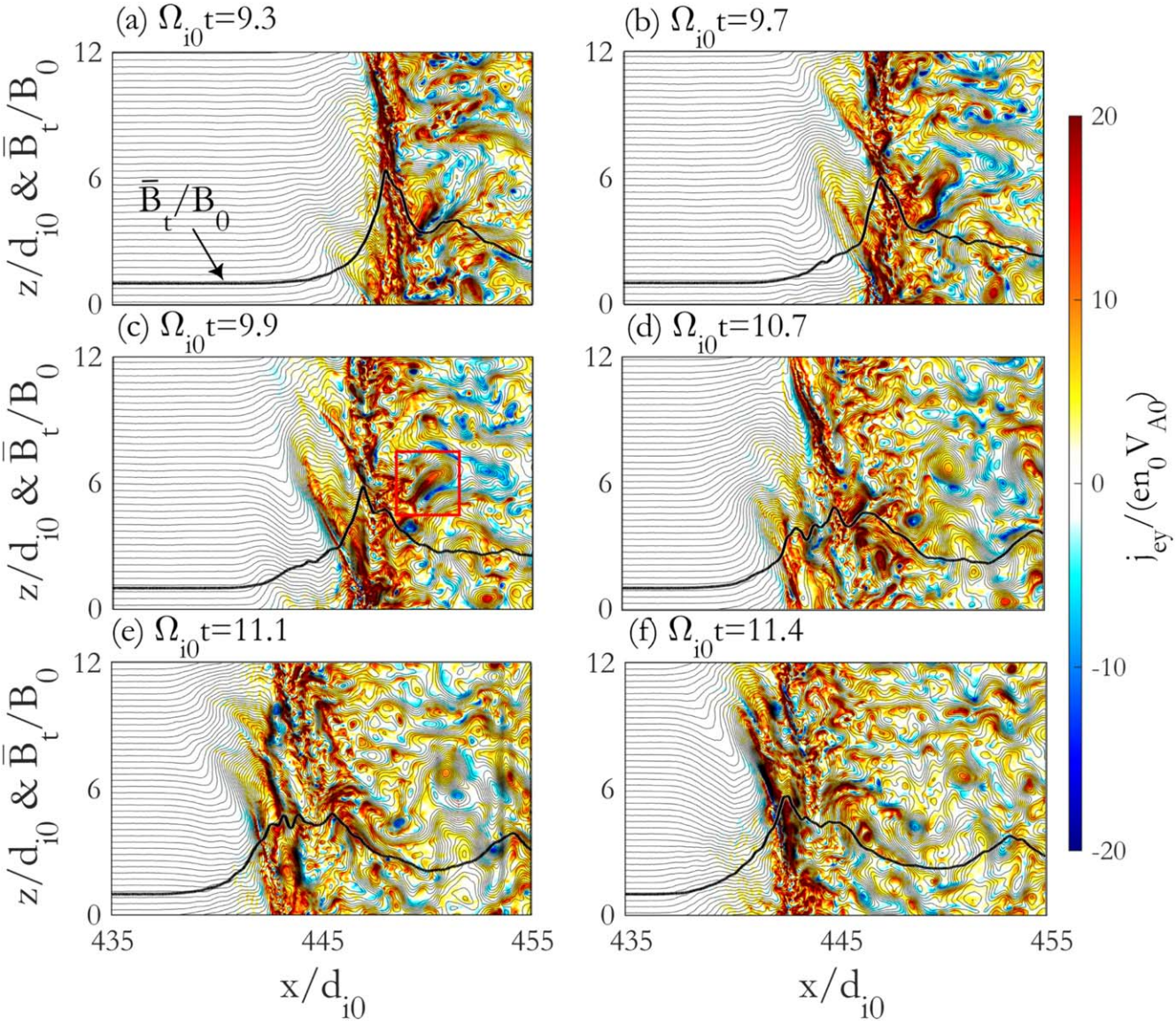


**Figure 2.** Magnetic field lines and electron current in the $y$ direction ($j_{ey}$) at $\Omega_{i0}t$ values of (a) 9.3, (b) 9.7, (c) 9.9, (d) 10.7, (e) 11.1, and (f) 11.4. The profiles of the average value of the magnetic field $\bar{B}_t$ are also plotted in the figure for reference.

well-known quadrupolar structure found in other simulations and satellite observations in the Harris current sheet (e.g., Fu et al. 2006; Huang et al. 2010; Wang et al. 2012). This may be caused by the curvature of magnetic field lines around the X line and fast evolution of the current sheets. The reconnection electric field $E_y'$ as well as $j_{ey}E_y'$ exist in the vicinities of the two X lines. The peak values of the reconnection electric field are about $2.6V_{A0}B_0$ and $-2.3V_{A0}B_0$ in current sheets CS1 and CS2, respectively. In Figures 3(e) and (f), we show that the electron outflows move along the $L_1$ and $L_2$ directions in the two current sheets. Here, the background electron flow in the two current sheets have been eliminated. Obviously, the two X lines are accompanied by the bidirectional high-speed electron outflows, and their speed may exceed the local Alfvén speed (here, the values of the local Alfvén speed are about $1.9V_{A0}$ and $1.8V_{A0}$, respectively).

Now we analyze in detail the characteristics of current sheet CS1, which is asymmetric. In the current sheet, the magnetic field and plasma density on the right side are $B_1 \approx 4.26B_0$ and $n_1 \approx 4.02n_0$, while those on the left side are $B_2 \approx 4.69B_0$ and $n_2 \approx 4.47n_0$. Therefore, the half-width and length of the current sheet are about 0.38 and 0.56 times the local ion inertial length, which is calculated based on the density $n_m = n_1B_2 + n_2B_1/B_1 + B_2 \approx 4n_0$. Equivalently, the half-width of the current sheet is about 3.04 times the local electron inertial length. The reconnection electric field normalized by $V_AB_m$ is about 0.26, where $B_m = 2B_1B_2/(B_1 + B_2) \approx 4.5B_0$ and $V_A^2 = B_1B_2/\mu_0 m_i n_m \approx 5.0$ (Cassak & Shay 2007). According to the results in Sharma Pyakurel et al. (2019), the ions do not response to magnetic reconnection when the length of the current sheet is comparable to the ion inertial length. Simultaneously, we also find that the lifetime of the current sheet is shorter than the ion cyclotron period based on $B_m(2^\pi/\Omega_{ci} \approx 1.39)$, as shown in Figure 4. Based on these considerations, only the electrons are involved in reconnection, and it is electron magnetic reconnection without ion coupling. Therefore, the reconnection electric field normalized by $V_{Ae}B_m$ (where $V_{Ae}^2 = B_1B_2/\mu_0 m_e n_m \approx 320$) is about 0.01.

The evolution of the current sheets in the region denoted by the red lines in Figure 2(c) is also investigated. Figure 4 plots the electron current in the $y$ direction $j_{ey}$ and the topology of the

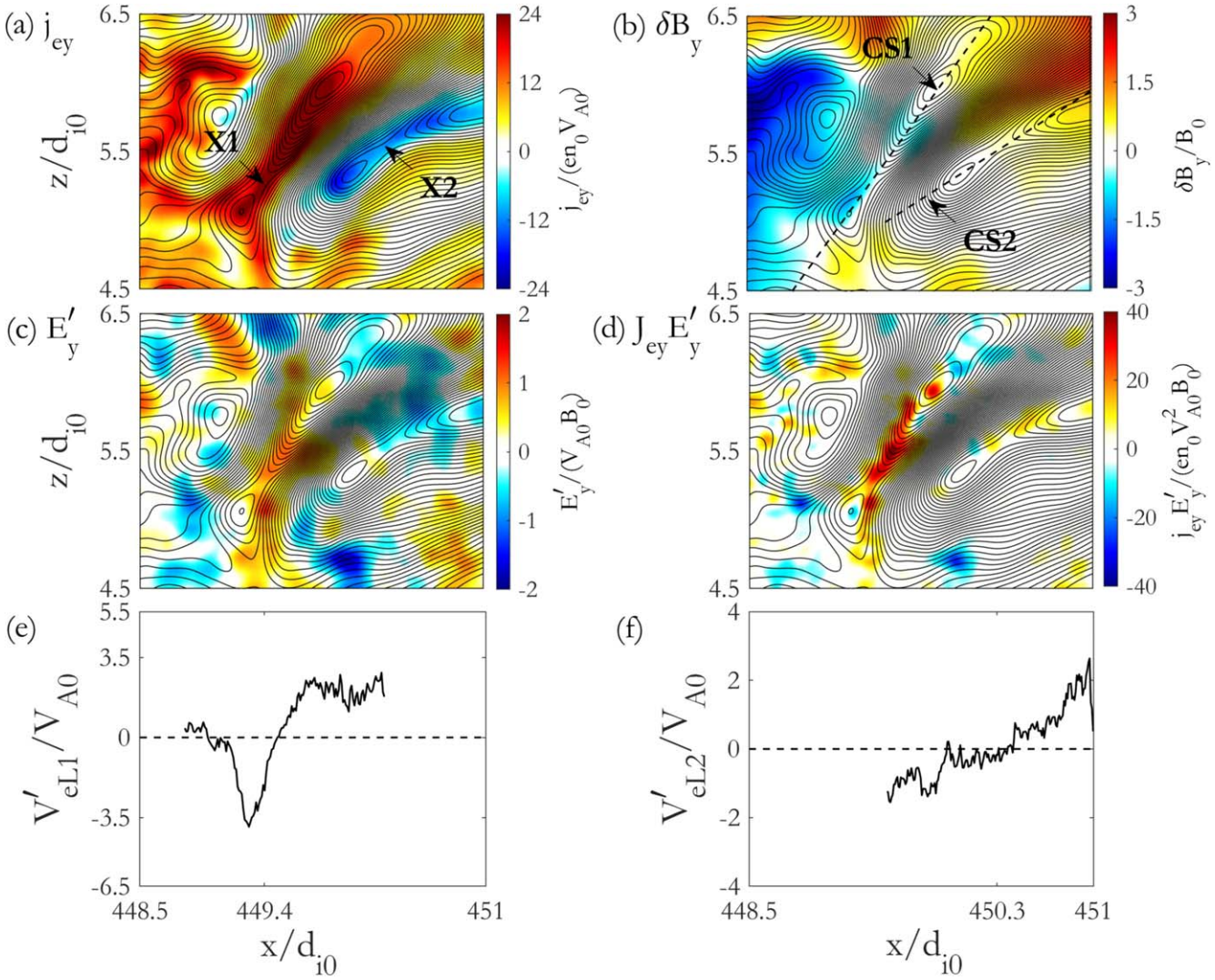


**Figure 3.** Enlarged view of the region denoted by the red lines in Figure 2(c). (a) Electron current in the $y$ direction $j_{ey}$, (b) fluctuating magnetic field in the $y$ direction $\delta B_y$ (where $\delta B_y = B_y - \tilde{B}_y$, and $\tilde{B}_y$ is the average value of $B_y$ in the denoted region), (c) electric field in the $y$ direction $E_y'$ (where $E' = E + V_e \times B$), and (d) $j_{ey}E_y'$ at $\Omega_{i0}t = 9.9$. In the figure, CS1 and CS2 denote the two current sheets. X1 and X2 denote the X points in current sheets CS1 and CS2. (e)–(f) show that the electron outflows move along the $L_1$ and $L_2$ directions in the two current sheets. Here, the background electron flow in the two current sheets has been eliminated.

magnetic field lines at $\Omega_i t = 9.9$, 10.1, 10.3, 10.5, 10.7, and 11.1 (also see the associated animation of Figure 4, which shows the time evolution of the two current sheets observed in the immediate downstream of the shock from $\Omega_i t = 9.6$ to 13.0). We still focus on the two current sheets denoted by CS1 and CS2. In each current sheet, two magnetic islands are formed around the X line, and they become gradually larger with the proceeding of magnetic reconnection. The sizes of these islands range from $1.2d_{i0}$ to $1.57d_{i0}$, or 1.74 to 2.26 times the local ion inertial lengths. The islands may also merge with other islands. Simultaneously, the two current sheets are largely distorted, or even break into several segments.

## 4. Conclusions and Discussion

In this paper, using a 2D PIC simulation model, we have studied magnetic reconnection associated with a quasi-perpendicular shock. The results showed that the quasi-perpendicular shock is nonstationary, and it experiences reformation with a cyclic period of about $2.1\Omega_{i0}^{-1}$. During the reformation of the shock, the magnetic field lines in the foot region are first bent upward and then squeezed. A current sheet is eventually formed. Because the width of the current sheet is on the electron scale, the electron motions are nonadiabatic, and the current is carried mainly by the electrons. The current sheet is convected to the shock front by the solar wind. After these structures interact with the shock front, the shock front becomes irregular. Both the current sheet carried by the solar wind and the current sheet associated with the shock front are distorted and fragmented into many filamentary current sheets in the shock transition region. Magnetic reconnection may occur in these filamentary current sheets, and magnetic islands are formed. Based on the width, length, and lifetime of these current sheets, we deduce that only electrons are involved in magnetic reconnection.

Electron magnetic reconnection without ion coupling has been observed by MMS satellites in the magnetotail (Wang et al. 2018) and magnetosheath (Phan et al. 2018). The observations by Phan et al. (2018) indicate that electron reconnection can occur in the downstream of a quasi-parallel shock. However, our results predict that electron magnetic reconnection may also occur in the transition region and downstream of a quasi-perpendicular shock, which could be verified by MMS observations in the future.

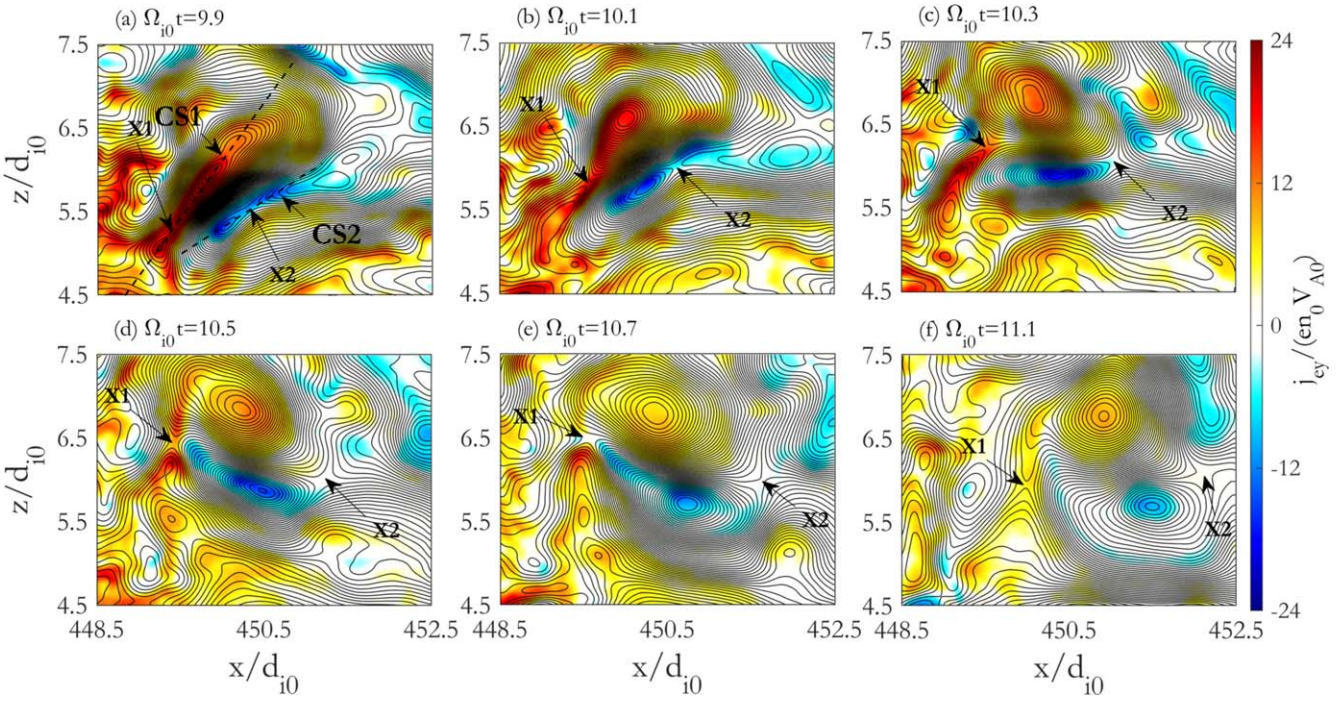


**Figure 4.** Electron current in the $y$ direction $j_{ey}$ and topology of the magnetic field lines at $\Omega_{i0}t$ values of (a) 9.9, (b) 10.1, (c) 10.3, (d) 10.5, (e) 10.7, and (f) 11.1. X1 and X2 in the figure stand for the X points in current sheets CS1 and CS2, which are shown in Figure 4(a). An animation of this figure is available. It shows the time evolution of the two current sheets observed in the immediate downstream from $\Omega_{i0}t = 9.6$ to 13.0. The real-time duration of the animation is 7 s.

(An animation of this figure is available.)

Please note that, in this paper, the simulation is performed in the $x$–$z$ plane, and the ambient magnetic field has a strong $y$ component. Therefore, magnetic reconnection in the shock transition region of the perpendicular shock has a strong guide field. How it will influence the energy dissipation in a quasi-perpendicular shock requires further investigation.

This work was supported by the NSFC Grants 41774169, 41804159, and 41874203, Key Research Program of Frontier Sciences, CAS (QYZDJ-SSWDQC010), and the Strategic Priority Research Program of Chinese Academy of Sciences, grant No. XDB 41000000. Z.Y. acknowledges partial support by the Specialized Research Fund for State Key Laboratories of China, Youth Innovation Promotion Association of the CAS (2017188), and the project of Civil Aerospace "13th Five Year Plan" Preliminary Research in Space Science (Project Name: Research on Important Scientific Issues of Heliospheric Boundary Exploration; project Nos. D020301 and D030202). Z.Y. appreciates helpful discussions with C. Huang from IGG. The computations were performed by the Numerical Forecast Modeling R&D and VR System of the State Key Laboratory of Space Weather and HPC of the Chinese Meridian Project.

## ORCID iDs

Quanming Lu https://orcid.org/0000-0003-3041-2682
Zhongwei Yang https://orcid.org/0000-0002-1509-1529
Rongsheng Wang https://orcid.org/0000-0002-9511-7660
Kai Huang https://orcid.org/0000-0003-3630-309X
San Lu https://orcid.org/0000-0003-2248-5072

## References

Angelopoulos, V., McFadden, J. P., Larson, D., et al. 2008, Sci, 321, 931
Arber, T. D., Bennett, K., Brady, C. S., et al. 2015, PPCF, 57, 113001
Baker, D. N., Peterson, W. K., Eriksson, S., et al. 2002, GeoRL, 29, 2190
Bessho, N., Chen, L. J., Wang, S., Hesse, M., & Wilson, L. B. 2019, GeoRL, 46, 9352
Cassak, P. A., & Shay, M. A. 2007, PhPl, 14, 102114
Dungey, J. W. 1961, PhRvL, 6, 47
Fu, X. R., Lu, Q. M., & Wang, S. 2006, PhPl, 13, 012309
Hada, T., Oonishi, M., Lembege, B., & Savoini, P. 2003, JGRA, 108, 1233
Hao, Y., Lu, Q., Gao, X., et al. 2014, JGRA, 119, 3225
Hao, Y., Lu, Q., Gao, X., & Wang, S. 2016, ApJ, 823, 7
Huang, C., Lu, Q., & Wang, S. 2010, PhPl, 17, 072306
Johlander, A., Schwartz, S. J., Vaivads, A., et al. 2016, PhRvL, 117, 165101
Lembege, B., & Savoini, P. 1992, PhFlB, 4, 3533
Lembege, B., & Savoini, P. 2002, JGRA, 107, 1037
Lu, Q., Wang, H., Wang, X., et al. 2020a, GeoRL, 47, e85661
Lu, Q., & Wang, S. 2006, JGRA, 111, A05204
Lu, S., Wang, R., Lu, Q., et al. 2020b, NatCo, 11, 5049
Matsukiyo, S., & Scholer, M. 2012, JGRA, 117, A11105
McKean, M. E., Winske, D., & Gary, S. P. 1992, JGR, 97, 19421
Paschmann, G., Papamastorakis, I., Sckopke, N., et al. 1979, Natur, 282, 243
Phan, T. D., Eastwood, J. P., Shay, M. A., et al. 2018, Natur, 557, 202
Pu, Z. Y., Zhang, X. G., Wang, X. G., et al. 2007, GeoRL, 34, L20101
Retinò, A., Sundkvist, D., Vaivads, A., et al. 2007, NatPh, 3, 236
Scholer, M. 1990, GeoRL, 17, 1821
Sharma Pyakurel, P., Shay, M. A., Phan, T. D., et al. 2019, PhPl, 26, 082307
Sonnerup, B. U. O., & Scheible, M. 1998, in Analysis Methods for Multi-Spacecraft Data, ed. G. Paschmann & P. W. Daly (Bern: Int. Space Science Institute), 185
Su, Y., Lu, Q., Huang, C., et al. 2012, JGRA, 117, A08107
Turner, D. L., Wilson, L. B., Goodrich, K. A., et al. 2021, ApJL, 911, L31
Vörös, Z., Yordanova, E., Varsani, A., et al. 2017, JGRA, 122, 11442
Wang, R., Lu, Q., Nakamura, R., et al. 2018, GeoRL, 45, 4542
Wang, R., Nakamura, R., Lu, Q., et al. 2012, JGRA, 117, A07223
Wang, S., Chen, L.-J., Bessho, N., et al. 2019, GeoRL, 46, 562
Winske, D., & Quest, K. B. 1988, JGR, 93, 9681
Yang, Z. W., Lembège, B., & Lu, Q. M. 2012, JGRA, 117, A07222
Yang, Z. W., Liu, Y. D., Johlander, A., et al. 2020a, ApJL, 901, L6
Yang, Z. W., Liu, Y. D., Matsukiyo, S., et al. 2020b, ApJL, 900, L24
Yang, Z. W., Lu, Q. M., Lembege, B., & Wang, S. 2009, JGRA, 114, A03111
Yordanova, E., Vörös, Z., Varsani, A., et al. 2016, GeoRL, 43, 5969